Cronfa - Swansea University Open Access Repository

_____

This is an author produced version of a paper published in:
Journal of Alloys and Compounds

_____

Cronfa URL for this paper:
http://cronfa.swan.ac.uk/Record/cronfa35713

_____

Paper:

_____

Accepted Manuscript

A novel High-Entropy Alloy-based composite material

Sephira Riva, Adam Tudball, Shahin Mehraban, Nicholas P. Lavery, Stephen G.R. Brown, Kirill V. Yusenko

Please cite this article as: S. Riva, A. Tudball, S. Mehraban, N.P. Lavery, S.G.R. Brown, K.V. Yusenko, A novel High-Entropy Alloy-based composite material, *Journal of Alloys and Compounds* (2017), doi: 10.1016/j.jallcom.2017.09.274.

Sephira Riva, Adam Tudball, Shahin Mehraban, Nicholas P. Lavery, Stephen G.R. Brown,

Kirill V. Yusenko[1*]

[1]College of Engineering, Swansea University, Bay Campus, Swansea SA1 8EN, Wales, UK

[2]Kennametal Manufacturing (UK) Ltd., Lake Road, Leeway Industrial Estate, Newport NP19 4SR,

Wales, UK

Correspondence:

Email: 839245@swansea.ac.uk (S.R.); k.yusenko@swansea.ac.uk (K.V.Y.)

Phone: +44 (0)1792205678 (K.V.Y.)

Abstract

This study reports the results of the addition of different reinforcing agents (*i.e.* nano-diamonds, SiC, Sc_2O_3, *h*-BN, *c*-BN and CN) on the sintering process of the *B2*-structured $Al_2CoCrFeNi$ High-Entropy Alloy. The best candidate for further thermal, electrical and mechanical characterisation was chosen to be the alloy containing 2 wt.% nano-diamonds. The composite was prepared using spark-plasma sintering of pre-alloyed powders and characterized with SEM-EDX, DSC, Laser Flash Analysis (LFA), electrical conductivity and Seebeck coefficient, dilatometry, Young's modulus, Vicker's hardness, 3-points flexural test. It shows unexpectedly low thermal expansion coefficient (from 3×10^{-6} to 17×10^{-6} K^{-1} between RT and 500 °C), high electrical resistivity and Seebeck coefficient and hardness comparable to the sintered blank $Al_2CoCrFeNi$.

Keywords: High-Entropy Alloys; Metal matrix composites; Spark plasma sintering; Nano-diamonds composite; Thermo-electric properties

unattainable within conventional alloys systems. With their inherent features being deeply influenced by the nature of the metal matrix and by the type and amount of secondary phase herein contained, MMCs are typically implemented for the thermal management of electronic components [1] and for applications requiring high hardness, yield and tensile strength [2]. The wide variety of reinforcing materials used, ranging from carbides (SiC, B_4C and WC) to oxides (Al_2O_3 and SiO_2) to carbon nanotubes and graphite, is matched by the diversity of metal matrices [3]. Commonly used metal systems include light metal alloys (Al, Mg and Ti), Zn- and Cu-based alloys and stainless steel, but Al remains by far the most exploited matrix material for the development of new MMCs [4]. Thus, most work reported in the literature refers to the A357, A359, 2618, 2214, 6061, 6063 and 7075 aluminium alloys [5]; [6]; [7].

Considering that the attractive properties of MMCs often entail tuneable thermal and mechanical properties, the absence of MMCs based on multicomponent alloys might appear surprising. However, a homogeneous distribution of the strengthening phase requires a careful balance of wettability and chemical affinity, which would be extremely difficult to achieve with complex multi-phase systems. An answer to this issue can come from the steadily growing field of High-Entropy Alloys (HEAs), multicomponent (≥ 5 elements) alloys with near equiatomic composition which combine high chemical complexity with simple, single-phase crystal structures [8]. Moreover, HEAs have been proposed for applications in which high thermal and mechanical stabilities are pivotal.

The model $Al_2CoCrFeNi$ HEA provides ideal background for the development of a new family of MMCs. Not only does $Al_2CoCrFeNi$ represent one of the few examples of purely single-phase *B2*-structured alloy, it also shows exceptional phase stability under extreme conditions of temperature and pressure and outstanding mechanical properties [9].

2

mechanical properties were characterized and compared to the blank Al$_2$CoCrFeNi HEA treated in the same way [10].

2. Experimental procedure

2.1 Preparation of the material

Al$_2$CoCrFeNi was prepared using induction melting from powders of pure metals. Samples were melted in *h*-BN crucibles in an Ar filled glove-box. Complete melting of the samples was achieved above 1300 °C. After 1-2 minutes at the melting temperature, the sample was cooled down naturally to room temperature. The sample was re-melted three times to ensure homogeneity. It was then powdered using a Fritsch Planetary Mill PULVERISETTE 5/2 (10 mm steel balls, ball-to-powder ratio 10:1, 36 h, 250 r.p.m.).

Samples of the obtained HEA powder were mixed with hexagonal boron nitride (*h*-BN, 3 wt.%, Sigma Aldrich), cubic boron nitride (*c*-BN, 2 wt.%, Kennametal Manufacturing), nano-diamonds (2, wt.%, Sigma Aldrich), silicon carbide (SiC, 2 wt.%, Sigma Aldrich), plasma functionalized multi-welled carbon nanotubes (CN, 1.5 wt.%, Haydale HDPlas® MWCN) or scandium oxide (Sc$_2$O$_3$, 0.5 wt.%, Fisher Scientific), using a Fritsch Planetary Mill PULVERISETTE 5/2 (10 mm steel balls, ball-to-powder ratio 5:1, 5 minutes, 250 r.p.m.). The average particle size of the additives was confirmed by laser diffraction with a Malvern Mastersizer 3000: the results are reported in Table 1. With respect to the standard 2 wt.% addition, *h*-BN was used in higher quantity than *c*-BN to study the effect of crystal structure as well as different concentration of additive on the HEA matrix. On the other hand, part of the originally weighted CN amount was lost during the loading process of the powder due to its volatility, giving a lower addition than originally planned. Finally, the low amount of Sc$_2$O$_3$ was due to its high cost and to the relatively low amount of aluminium which will be necessary to reduce it to scandium metal.

3

All powders were sintered using a FCT System GmbH Spark Plasma Sintering Furnace type H-HP D 250 located at Kennametal Manufacturing (UK) Ltd. Powders were hot-pressed in vacuum 50°/min and 7.8 MPa/min until 850 °C, then maintained at 850 °C for 10 min under a 50 MPa load. Throughout the heating phase, a repeated pulsed DC current scheme 36ms/8ms on/off was used [11].

2.2 Material characterization

All samples were mounted in carbonised resin, polished using MetaDiTM Supreme Polycrystalline Diamond Suspension (Buehler, Esslingen am Neckar, Germany) (1 μm) and etched with a 5% solution of HNO_3 in ethanol. Morphology and elemental composition were analysed using a Hitachi S-4800 Field Emission scanning-electron microscope (SEM, Hitachi, Tokyo, Japan) equipped with energy dispersive X-ray (EDX) analyser. The average elemental composition was obtained from 2.5 x 1.5 mm maps and locally. Density was measured using flotation in distilled water with the ATTENSION tensiometer. Results are an average of five measurements performed at 25 °C. Theoretical density was calculated with the Rule of Mixtures, using elemental composition values obtained from the EDX maps.

The following measurements were performed on specimens of the spark-plasma sintered $Al_2CoCrFeNi$ and $Al_2CoCrFeNi$ +2wt.% nanodiamonds. Differential scanning calorimetry (DSC) measurements were performed on small pieces of sintered samples (50 mg) placed in an Al_2O_3 crucible and heated in a Netzsch STA 449F1. Heating and cooling were performed in flowing Ar gas with a temperature ramp of 10 °C·min^{-1} from 35 to 850 °C. 10x10x3mm square samples were tested for thermal diffusivity using a NETZSCH LFA 457 laser flash analyzer [12]. Samples were measured for thickness and then coated with graphite to increase absorption of laser energy and

4

set to be 50 to 850 °C with 50° increments, 3 shots were taken at each temperature and the individual diffusivity results measured and then averaged. All measurements were performed in Ar atmosphere. Specific heat capacity for thermal conductivity calculation is determined by the software using the Pyroceram reference according to the following relation:

$$C_P^{sample} = \frac{T_\infty^{ref} \cdot Q^{sample} \cdot V^{sample} \cdot \rho^{ref} \cdot D^{ref} \cdot d_{sample}^2 \cdot C_p^{ref}}{T_\infty^{sample} \cdot Q^{ref} \cdot V^{ref} \cdot \rho^{sample} \cdot D^{sample} \cdot d_{ref}^2}$$

where T_∞^{ref} and T_∞^{sample} correspond to the heat loss corrected voltage increase of detector signal at infinite time for the reference and the sample respectively; Q^{ref} and Q^{sample} is the energy (integral of the laser pulse) on the reference and sample respectively; V^{ref} and V^{sample} is the reference (or sample) amplification factor; ρ^{ref} and ρ^{sample} are the density of the reference and the sample respectively; D^{ref} and D^{sample} are the reference and sample respective thicknesses; d_{ref}^2 and d_{sample}^2 are the orifices area of reference and sample; C_p^{ref} is the tabulated value of specific heat capacity for the reference material. The change in density following heating was considered by using the thermal expansion data from the dilatometry experiment outlined above. Temperature dependent electrical resistivity and Seebeck coefficients were measurements on a Seebeck coefficient/Electrical resistance measuring ZEM-3 system (Advanced RIKO, Inc.) equipped with a SDC35 temperature controller (Yamatake), a 2010 multimeter (Keithley®) and a R6146 programmable DC voltage/current generator (ADVANTEST). Resistivity was measured with a 4-points probe method by sending current through the sample and simultaneously measuring the voltage difference along the specimen's length. The Seebeck coefficient was obtained by heating one end of the sample and simultaneously measuring the voltage generated between probes. The specimens were tested every 50 °C (ΔT=10, 20, 30 and 40 °C) from 50 to 800 °C with a type R thermocouple (Pt-13 % Rh *vs* Pt). Linear thermal expansion ΔL/L$_0$ (accuracy 0.003 %) was

5

the specimens was measured with the pulse-echo ultrasound technique using an Olympus ultrasound generator. The speed of sound in the sample material was measured in a longitudinal and shear direction. To achieve coupling between the contact transducer and the specimen we used glycerin (longitudinal waves) and molasses (shear waves). Vickers hardness was measured on a WilsonR VH3100 Automatic Knoop/Vickers Hardness tester. 25 individual points under 9.81 N (1 kg) testing load were measured to obtain statistically significant results. Three-point flexural tests were undertaken using a Tinius Olsen H25KS with a 25kN maximum load cell. The span of the support pins was 30mm and the radius of the rollers 6mm. The loading pin was moved at a rate of 1mm/per minute. Rectangular-shaped specimens with 40x4x4mm dimensions were tested.

3. Results

The current study presents preliminary results obtained while investigating the $Al_2CoCrFeNi$ HEA as a potential metal matrix for composite materials. The effect of different reinforcing agents (*i.e.* nano-diamonds, SiC, Sc_2O_3, *h*-BN, *c*-BN and CN) on the sintering process was evaluated to select a candidate for further characterization and development. The blank *B2*-structured $Al_2CoCrFeNi$ underwent the same sintering process as its composites, whose compositions are reported in Table 1.

Table 1. Overview of the sintered samples. The acronym "HEA" stands for the $Al_2CoCrFeNi$ High-Entropy Alloy.

Sample code	Composition according to EDX maps (at.%)					Nominal material addition	Average particle size additive	Theo density (gcm^{-3})	Density (gcm^{-3})
	Al	Co	Cr	Fe	Ni				

6

HEA +SiC	36.9(5)	14.5(3)	26.4(5)	10.5(2)	11.5(1)	2 wt.%	20 µm	6.93	5.03(7)
HEA +Sc$_2$O$_3$	49.4(7)	5.9(5)	10.6(4)	10.1(2)	23.7(1)	0.5 wt.%	20 µm	6.58	5.26(7)
HEA +h-BN	36.2(3)	15.6(2)	16.2(2)	16.9(2)	14.8(2)	3 wt.%	10 µm	7.21	5.26(8)
HEA +c-BN	45.8(4)	14.7(4)	11.9(2)	15.8(3)	11.6(3)	2 wt.%	50 µm	6.72	5.63(6)
HEA +CN	31.4(6)	17.6(6)	19.3(4)	19.2(4)	12.7(2)	1.5 wt.%	NA	7.21	NA

Composites created to achieve high-performance thermal management materials traditionally employ diamonds, silicon carbide or carbon nanotubes as additives [13]. Diamond is selected as a high quantity filler because it is an isotropic material with record thermal conductivity (up to 2200 $Wm^{-1}K^{-1}$ for pure monocrystals) and due to its thermal expansion coefficient in metal matrix composites (MMCs), which is comparable to the one of semiconductor elements [14]. Equally high thermal conductivity is realized in silicon carbide particle reinforced aluminium [15]. Finally, carbon nanotubes have attracted much attention as promising reinforcements for MMCs due to their high strength and electrical/thermal conductivities [16]; [17]. The addition of Sc$_2$O$_3$ to the HEA was justified from the need to find a cheaper route to achieve the addition of scandium in the HEA system, which is known to enhance phase stability and mechanical properties [18]. Lastly, boron nitride is characterized by low dielectric coefficient and extreme thermal shock resistance, which make it an attractive addition to composite ceramics or to metal alloys [19]; [20]; [21].

All samples were spark plasma sintered into disks of 8 cm diameter and 5 mm thickness; but none of the specimens except the HEA and HEA +2 wt.% nano-diamonds retained their shape. The poor sintering of SiC-, Sc$_2$O$_3$-, BN-containing samples was confirmed by density measurements (Table 1), displaying up to a 20 % density decrease in comparison with the HEA sample. All specimens display lower density with respect to the calculated theoretical values. Density measurement of the HEA +1.5 wt.% CN sample was impossible due to its extreme fragility.
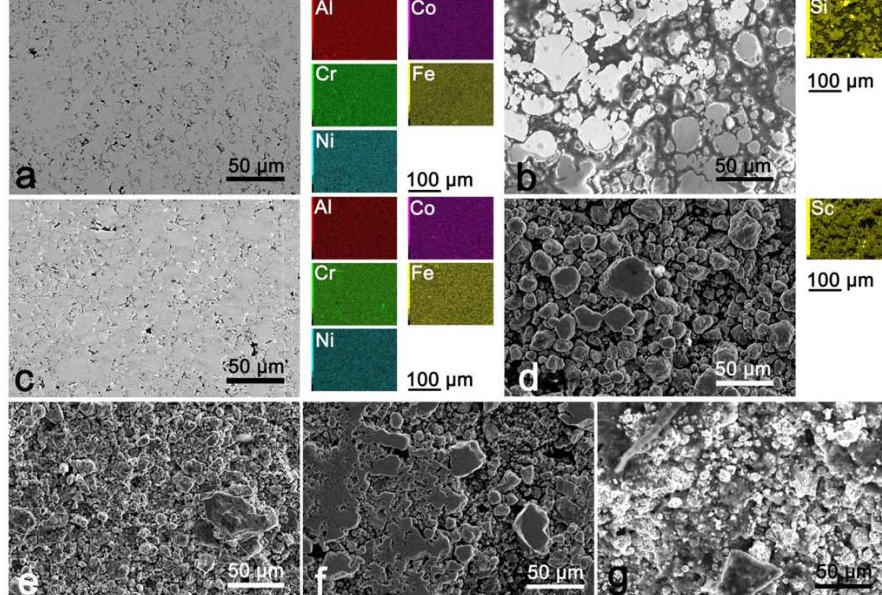
7

Figure 1- SEM and selected EDX micrographs of (*a*) Al$_2$CoCrFeNi HEA with element distribution maps; (*b*) Al$_2$CoCrFeNi + 2wt.% SiC with a distribution map of Si in the sample; (*c*) Al$_2$CoCrFeNi +2 wt.% nano-diamonds with element distribution maps of the HEA matrix; (*d*) Al$_2$CoCrFeNi +0.5 wt.% Sc$_2$O$_3$ with a distribution map of Sc in the sample; (*e*) Al$_2$CoCrFeNi +3 wt.% h-BN; (*f*) Al$_2$CoCrFeNi +2 wt.% c-BN; (*g*) Al$_2$CoCrFeNi +1.5 wt.% CN.

Spark-plasma sintering of HEA powder of 5-20 µm particle size results in homogeneous element distributions (Figure 1a). Despite intergranular porosity, grain growth has occurred with respect to the original particle size [22]. Nevertheless, due to porosity the density of the spark-plasma sintered sample is only 92.5 % of the density of the thermally annealed sample prepared at the same temperature ($d_{f,\ ann}$ = 6.4(1) g·cm^{-3} and $d_{f,SPS}$ = 5.92(7) g·cm^{-3} as established from flotation; $d_{XRD,\ ann}$ = 6.33(1) g·cm^{-3} and $d_{XRD,\ SPS}$ = 6.24(1) g·cm^{-3} as estimated from PXRD data) [9]. An equally homogeneous element distribution is displayed by the nano-diamond-containing HEA (Figure 1c). Nano-diamonds are not identifiable from composition maps, but SEM highlights the presence of a dark-coloured phase along grain boundaries. Unfortunately, the nanodiamonds dimensions fall

8

clearly display the *B2* phase of the matrix and a second phase which can be indexed as diamond (Figure S6). We can therefore hypothesize that nano-diamonds are not subsumed by the matrix, but appear as inclusions [23], a result consistent with the previously reported absence of chemical bonding between diamonds and Al metal matrix in composites [24]. In the case of the SiC-containing sample (Figure 1b), the HEA demonstrates minimal capacity to penetrate the silicon clusters. This might be partly due to the low homogeneity of the starting powder (Figure S2). It has been postulated that the incomplete densification of large elemental clusters is a result of entrapped gases and/or localized increases in electrical resistivity [11]; [25]. Higher temperature and pressure might force the matrix into these features and encapsulate the SiC particles.

The traditional route to produce the commercially available Al-Sc master alloy makes use of the cheaper Sc_2O_3 as scandium source and exploits the reduction of the precursor with Al to form Al_2O_3 as by-product [26]. Nevertheless, while the studied HEA contains over 30 % Al, the conditions of temperature and pressure used are not enough to achieve the dissolution of the oxide in the HEA matrix following the formation of metallic scandium, or sample densification (Figure 1d).

BN and CN-reinforced materials (Figure 1e, 1f and 1g) show exceptionally poor densification behaviour even for very small additions. The poor performance of BN-bearing systems is likely connected to the high dielectric strength of BN (374 kV mm^{-1}), but hexagonal and cubic BN (respectively added as 3 wt.% and 2 wt.%) show quite different densification, quantifiable as a 6 % density difference [27].

Out of the seven evaluated composites, only HEA +2 wt.% nano-diamonds exhibited the desired response to SPS in terms of density and elemental distribution. As such, this sample and the blank HEA were the subject of further thermal, electrical and mechanical characterisation.

3.1 Thermoelectric properties

9

different (Figure 2). While the as-cast alloy presents a sigmoid-like reversible transition between 850 and 950 K, corresponding to the *B2* to *fcc* phase transformation, the signal is not present in either of the sintered samples [9]. The absence of phase transition in the interval make the system promising for further thermal and electrical characterization.
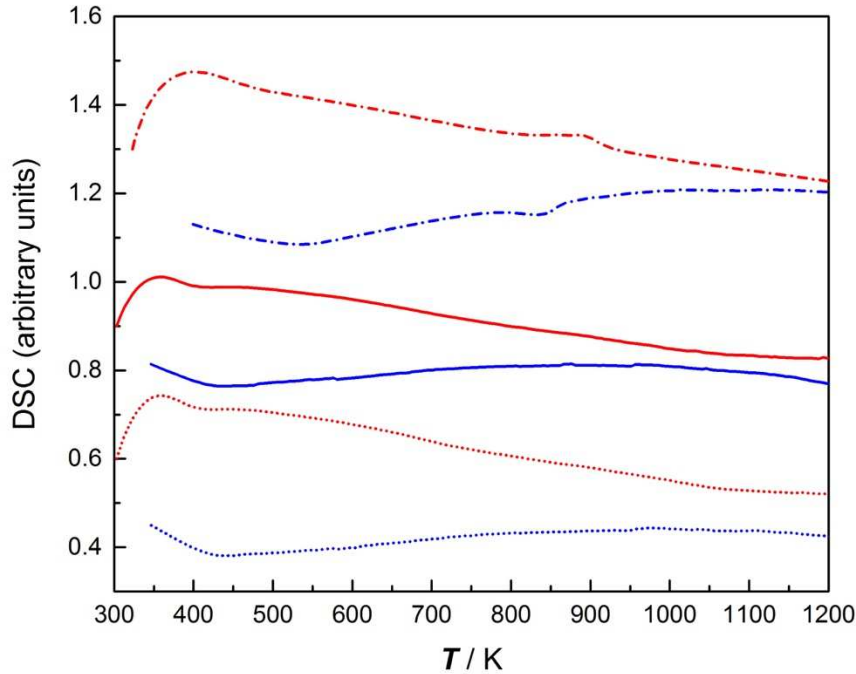

Figure 2: Differential scanning calorimetry (300-1200 K, 10 K min^{-1}) of as-cast Al$_2$CoCrFeNi (*short dash*), spark-plasma sintered Al$_2$CoCrFeNi powder (*solid line*) and Al$_2$CoCrFeNi composite material containing 2 wt.% nano-diamonds (*dotted line*). Heating and cooling cycles are reported in red and blue respectively.

Diamond-reinforced aluminium composites have been proposed as promising materials for the thermal management of electronic components, due to their ideal combination of high thermal (k) and electric (σ) conductivity and low coefficient of thermal expansion (*CTE*). Thermal conductivity values as high as 600 W m^{-1}K^{-1} and 552 W m^{-1}K^{-1}, combined with very low *CTE* (7-7.5 $\times$ 10^{-6} K^{-}

10
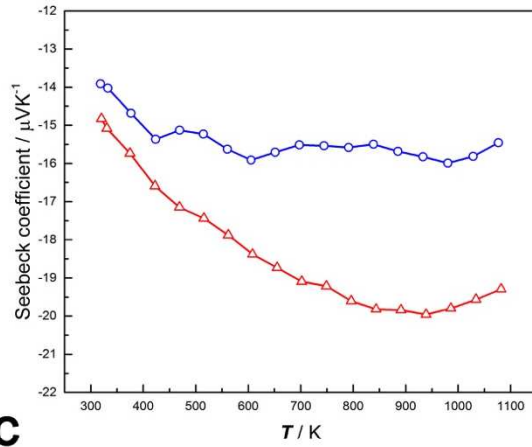
On the other hand, as cast high-entropy alloys typically have electrical resistivity between 100 and 220 µΩ·cm, which are values much higher than conventional alloys and comparable with bulk metallic glasses [30].
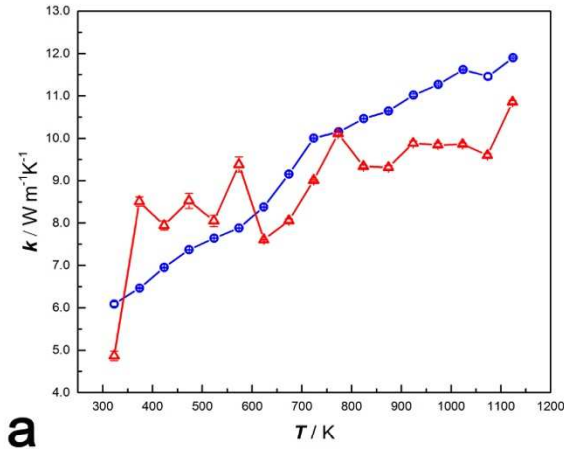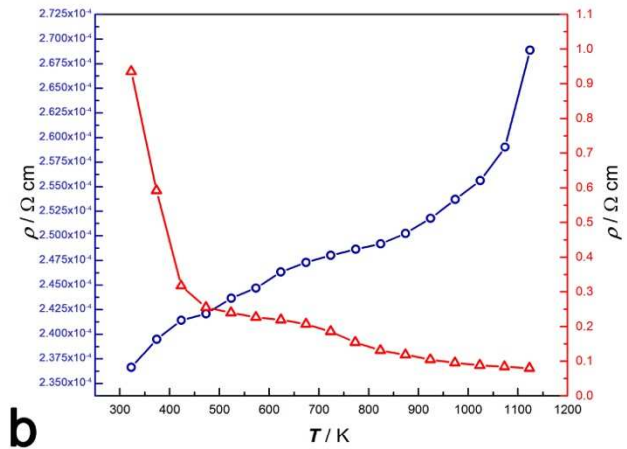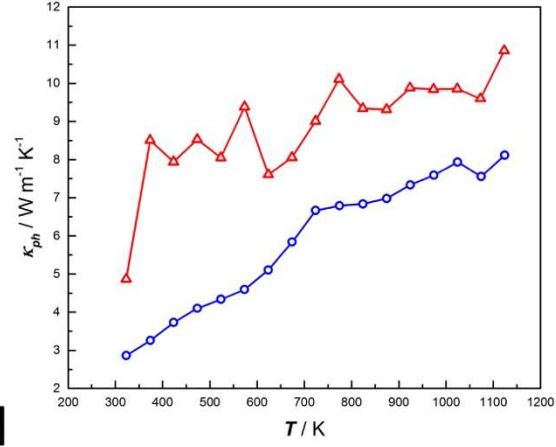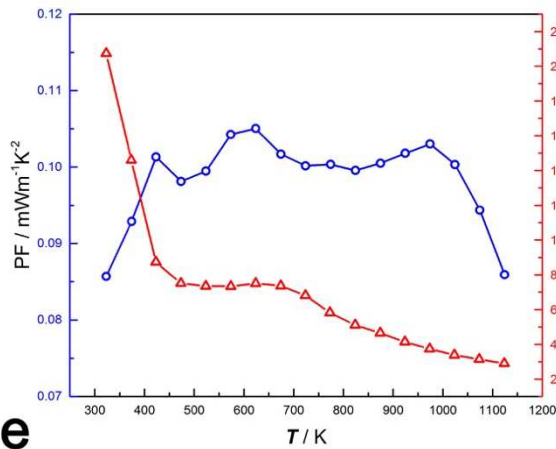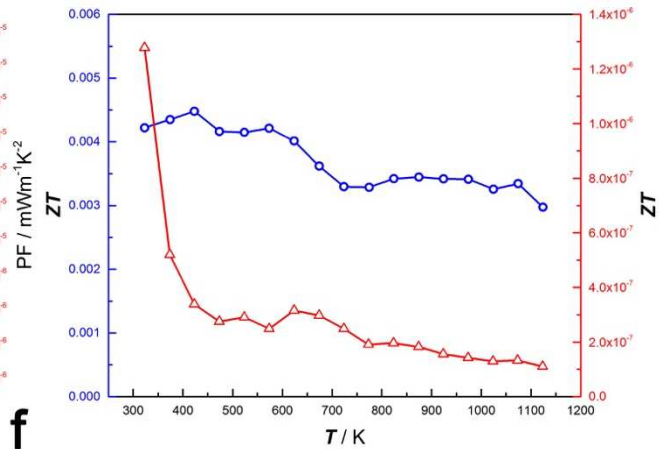
thermal conductivity (error for each measurement is shown as error bar); (*b*) electrical resistivity; (*c*) Seebeck coefficient; (*d*) calculated phononic contribution to the global thermal conductivity; (*e*) calculated power factor; (*f*) thermoelectric figure of merit ZT.

Figure 3 reports an overview of the thermal and electrical properties of the two specimens.

The sintered $Al_2CoCrFeNi$ HEA shows an electric resistivity of 225.84 µΩ·cm at 300 K, in good agreement with the value of 211.29 µΩ·cm at 300 K previously reported for the same as-cast alloy in pellet form (Figure 3b) [31]. The corresponding electrical conductivity is thus slightly lower than that previously reported for the $Al_2CoCrFeNi$ HEA [32]. Electrical resistivity is constant below 850 K - a feature which might arise from electron scattering from a complex microstructure and magnetic clusters -, while it increases linearly with temperature above 850 K. The low carriers' concentration (10^{19}-10^{21} cm^{-3} between 4-300 K), decreasing with temperature, and the high lattice distortion typical for HEAs support the hypothesis of electrical resistivity being affected by phonon scattering above the Debye temperature of the alloy. Electrical resistivity of the nano-diamond composite shows the opposite trend and decreases very steeply between 300 and 400 K [33]. The specimen behaves like a semiconductor, a feature which has not been observed for diamond-containing MMCs before. The electrical resistivity of the composite is much higher in comparison with the standard HEA, as is expected considering the loss of mean free path following the introduction of the additive.

Lattice distortion and low carrier concentration are also the main reason for the increase of thermal conductivity with temperature in HEAs. This behaviour is opposite to the one shown by most of pure metals in which the increase in lattice vibrations following heating result in electron scattering whose decreased mobility causes the decrease in thermal conductivity [30]. High-entropy alloys of the $Al_xCoCrFeNi$ series have been found to have low but diverse thermal conductivity (from 0.47

12

K respectively, Figure 3a).

The average Seebeck coefficient values for the two systems are reported in Figure 3c. Both composition appear to be *n*-type. While the absolute value of the Seebeck coefficient is almost constant for the HEA, it increases over a wide temperature range for the composite, reaching a maximum at 940 K (~20 μVK^{-1}).

The phononic contribution to thermal conductivity can be estimated from the Wiedemann-Franz law:

$$\kappa_{ph} = k_{tot} - \kappa_e = k_{tot} - (L\sigma T)$$

where *L* is the Lorentz number (2.44·10^{-8} WΩK^{-2}), σ the electrical conductivity and *T* the absolute temperature. As shown in Figure 3d, the phononic contribution is higher for the composite than for the pure alloy on the whole temperature range. This result can be ascribed to the presence of lattice scattering points on the interface between alloy and diamonds as well as to the sintering technique. From the power factors (σS^2) and thermoelectric figure of merit ZT ($\sigma S^2 T/k$) reported in Figures 3e and 3f, it is clear that the higher absolute Seebeck coefficient value of the composite specimen cannot overcome its very low electrical conductivity, making it unsuitable as thermoelectric material.

3.2 Thermal expansion

The experimental data shown in Figure 4a clearly show that the relative length changes *ΔL/L₀* are not linearly dependent with temperature over the studied range.
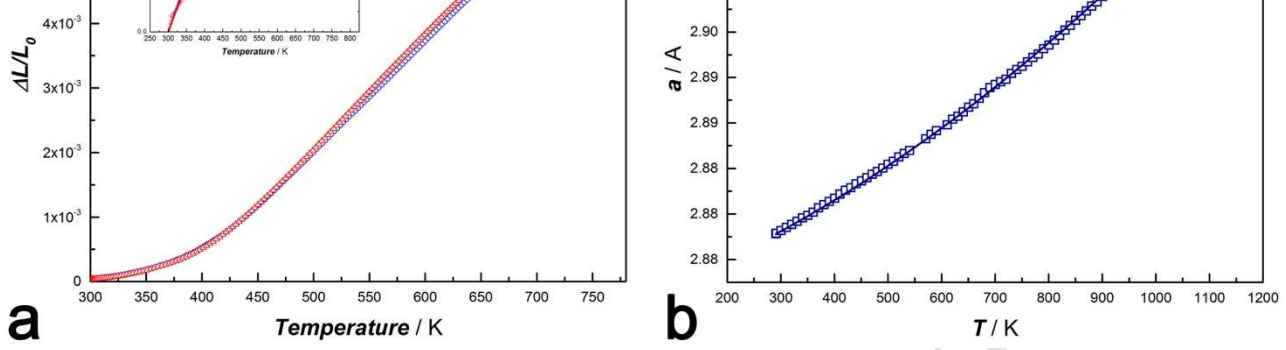
13

Figure 4 – (*a*) Thermal expansion of the Al$_2$CoCrFeNi HEA (*blue*) and of its composite material containing 2 wt.% nano-diamonds (*red*) after spark-plasma sintering. *Inset*: thermal expansion coefficient from 300 to 770 K, (*circles*) obtained as CTE_m and (*line*) obtained as thermal expansivity. (*b*) Thermal expansion of the cell parameter *a* from PXRD of the as-cast Al$_2$CoCrFeNi HEA (DIAMOND Light Source, I11, λ=0.494984 Å). Database fitting performed with equation (2).

Thermal expansion curves for the two materials can be fitted over the range 300 to 770 K with a polynomial equation of the type [36]:

$$\frac{\Delta L}{L_0} = a + b \cdot (T - T_0) + c \cdot (T - T_0)^2 + d \cdot (T - T_0)^3 + e \cdot (T - T_0)^4 \tag{1}$$

Where L is the sample length, L_0 the sample length at the starting temperature, T_o is the starting and T is the absolute temperature. Using the fitted data for $\Delta L/L_0$, values of thermal expansion coefficients defined as $CTE = \frac{1}{L_0}\frac{dL}{dT}$ (also referred to as *thermal expansivity*) or as $CTE_m = \frac{1}{L_0}\frac{\Delta L}{\Delta T}$ (also referred to as *average thermal expansion coefficient*) can be calculated [37]. They are reported as insert in Figure 4a in the range 300 to 770 K.

The expansion coefficient evaluated for Al$_2$CoCrFeNi by *in situ* high-temperature PXRD measurements (Figure 4b) [9], can be obtained by fitting the corresponding dataset to:

$$a(T) = a_{T_0} \cdot exp\left[\alpha \cdot (T - T_0) + \frac{\beta}{2} \cdot (T^2 - T_0^2)\right] \tag{2}$$

14

deviate from these values below 650 K; the effect of porosity is prominent at low temperature, and only above 650 K do the specimens behave as bulk materials. Subsequent cycles of heating and cooling reduce the hysteresis between the two curves and lead to thermal expansion values closer to lattice values above 400 K.

3.3 Mechanical properties

Three-point flexural stress tests (Figure 5) show a marked brittleness increase following the addition of nano-diamonds to the HEA.
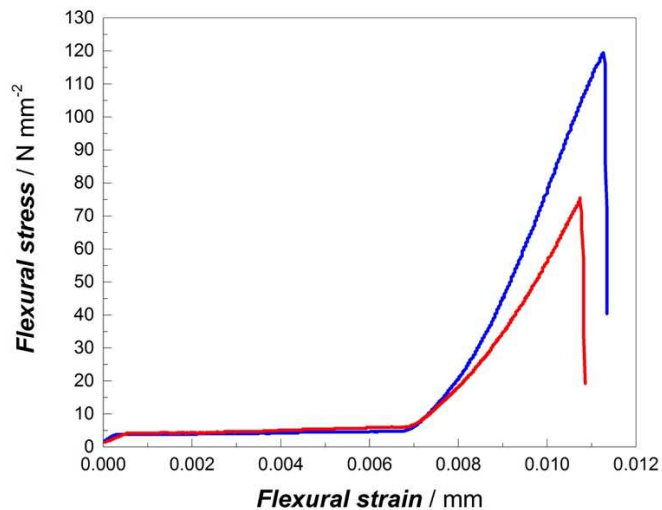

Figure 5 - Flexural stress-strain of the Al$_2$CoCrFeNi HEA (*blue*) and of its composite material containing 2 wt.% nano-diamonds (*red*) after spark-plasma sintering in a three-points setup.

This result might appear contradictory to Vicker's hardness results, which highlight no variation between the two samples; however, it should be noted that mechanical properties are just as dependent on internal non-homogeneity as thermal and electrical properties are. The presence of cavities and the uneven distribution of nano-diamonds are the reason behind of the high errors in hardness measurements (Table 2). The HEA and HEA +2 wt.% nano-diamond systems were

15

ratio through the following relations:

$$E = 2\rho c_S^2(1 + \nu) = \rho c_L^2 \frac{(1+\nu)(1-2\nu)}{1-\nu} \tag{3}$$

$$\nu = \frac{1 - 2 \cdot \frac{c_S^2}{c_L^2}}{2 - 2 \cdot \frac{c_S^2}{c_L^2}} \tag{4}$$

Where ρ is the material density, and c_S and c_L are the speed of shear and longitudinal wave in the material respectively. Table 2 lists the Poisson's ratio (ν), Young's modulus (E) and shear modulus (G) for the sintered HEA and HEA nano-diamond composite as determined from ultrasounds measurements.

Table 2. Overview of the mechanical properties of the Al$_2$CoCrFeNi HEA after spark-plasma sintering and of its composite material containing 2 wt.% nano-diamonds.

Sample	Maximum displacement (mm)	Poisson's ratio (ν)	Young's modulus (E)	Shear modulus (G)	Vicker's hardness (HV)
HEA	0.0113	0.2232	131.58 GPa	53.82 GPa	353 $\pm$43
HEA + nano-diamonds	0.0107	0.2366	117.22 GPa	47.40 GPa	337 $\pm$30

Unsurprisingly, the addition of nano-diamonds results in a decrease in the material elasticity. The reported Young's modulus values are consistent with those reported in the literature for other HEA systems [38]; [39]. With respect to the HEA, the composite is thus more brittle with a decrease in Young's modulus and comparable Poisson's ratio.

16

Trials performed via spark-plasma sintering using hexagonal or cubic boron nitride, carbon nanotubes, silicon carbide and scandium oxide as additives failed due to their low affinity with the matrix. The addition of 2 wt.% nano-diamonds, on the other hand, resulted in a compact composite with good machinability. However, the presence of residual porosity in the sintered $Al_2CoCrFeNi$ and its nano-diamonds composite (highlighted by microscopy, density and thermal expansion results) emphasizes the unsuitability of spark plasma sintering for the densification of HEA powders. In fact, densification by SPS is promoted by the flow of current between metallic particles, and HEAs have been reported as having higher electrical resistivity values in comparison with conventional alloys. Electrical resistivity is even higher for the nano-diamond composite, and it is thus not surprising that in both samples only limited grain growth occurs with respect to the original particle size. Plastic deformation and ultimately densification require appreciable inter-particle bonding which, in the case of the investigated system, is strongly dependent on heating conditions, rather than the applied pressure [9]. Considering that no phase transition appears between room temperature and 1200 K, complete densification might occur at higher temperature. This is also suggested by the comparison between macroscopic thermal expansion (*dL*) curves of the composites and lattice thermal expansion of the as-cast material: subsequent cycles of heating and cooling reduce the hysteresis between the two curves, and ultimately both composite behave as the original bulk material. In the first heating cycle, on the other hand, values of *dL* obtained for the composite specimen are much lower than those for lattice expansion; consistent with the presence of porosity and localized non-homogeneities.

Even though the sintered $Al_2CoCrFeNi$ HEA and its nano-diamond composite have similar thermal behaviour, they strongly differ in terms of electrical properties. Both samples display high electrical resistance due to the high lattice distortion typical of multi-principal component alloys and by the loss of mean free path following the introduction of the additive. The phononic contribution to

17

composite.

The addition of nano-diamonds is accompanied by a decrease in the material's elasticity, a slight increase in Poisson's ratio and a drop in Young's modulus, as well as a loss of ductility. The two samples have the same hardness, within experimental error.

5. Conclusions

The successful synthesis of the first example of an HEA-matrix composite, consisting of the *B2*-structured $Al_2CoCrFeNi$ HEA and 2 wt.% nano-diamonds is reported. The specimen was obtained via spark-plasma sintering of pre-alloyed powders and its thermal and mechanical properties were tested with respect to the similarly treated HEA sample.

The two materials display similar thermal properties (thermal expansion, thermal conductivity), but very different electrical features. These arise from the nature of the additive: as such, electrical resistivity decreases with increasing temperature, and Seebeck coefficient value is not constant over the temperature range, but increases steadily reaching a maximum at 940 K ($\sim$20 μVK^{-1}). Unfortunately, the higher Seebeck coefficient value of the composite cannot overcome its very low electrical conductivity, making it unsuitable as a thermoelectric material. The addition of nano-diamonds also affects mechanical properties, by increasing the brittleness of the sample and decreasing its elasticity.

The poor thermal and mechanical performances of the composite can be ascribed to the presence of residual porosity and to the low degree of affinity between the additive and the matrix. Nevertheless, a careful tuning of sintering temperature, additive type and quantity might open the door to a new generation of metal-matrix composites based on HEAs.

References

1. X.-H. Qu, L. Zhang, M. Wu, S.-B. Ren, Review of metal matrix composites with high thermal conductivity for thermal management application, Progress in Natural Science: Mater Intern 21 (2011), 189-197.

2. I.A. Ibrahim, F.A. Mohamed, E.J. Lavernia, Particulate reinforced metal matrix composites – a review, J. Mater. Sci. 26 (1991), 1137-1156.

3. M.O. Bodundrin, K.K. Alaneme, L.H. Chown. Aluminium matrix hybrid composites: a review of reinforcement philosophies; mechanical, corrosion and tribological characteristics, J. Mater. Res. Tech. 4 (2015), 434-445.

4. D.K. Das, P.C. Mishra, S. Singh, S. Pattanaik, Fabrication and heat treatment of ceramic-reinforced aluminium matrix composites – a review, Int. J. Mech. Mater. Eng. 9 (2014).

5. K.K. Alaneme, A.O. Aluko. Fracture toughness (K_{1C}) and tensile properties of as-cast and age-hardened aluminium (6063)-silicon carbide particulate composites, Scientia Iranica 19 (2012), 992-996.

6. T.V. Christy, N. Murugan, N. Kumar, A comparative study on the microstructures nd mechanical properties of Al 6061 alloy and the MMC Al 6061/TiB2/12p, J. Miner. Matls. Charac. Eng. 9 (2010), 57-65.

7. B. Hwu, S. Lin, M. Jahn, Effect of process parameters on the properties of squeeze cast SiCp-6061 Al metal matrix composite, Mater. Sci. Eng. A 207 (1996), 135-141.

9. S. Riva, W.A. Crichton, K. Spektor, A. Yudban, I. Kupenko, S. Klemme, F. Mazzali, S. Margadonna, N.P. Lavery, S.G.R. Brown, K.V. Yusenko, High-pressure high-temperature tailoring of high entropy alloys for extreme environments, Acta Mat. 2017 – *submitted*.

10. P.F. Yu, L.J. Zhang, H. Cheng, H. Zhang, M.Z. Ma, Y.C. Li, G. Li, P.K. Liaw, R.P. Liu, The high-entropy alloy with high hardness and soft magnetic property prepared by mechanical alloying and high-pressure sintering, Intermetal. 60 (2016), 82-87.

11. G.A. Sweet, M. Brochu, R.L. Hexemer Jr, I.W. Donaldson, D.P. Bishop, Consolidation of aluminum-based metal matrix composites via spark plasma sintering, Mater. Sci. Eng. A 648 (2015),123-133.

12. M. Kövér, M. Behúlová, M. Drienovsky, P. Motyčka, Determination of the specific heat using laser flash apparatus. J. Thermal Analysis Calorimetry 122 (2015), 151-156.

13. I. Firkowska, A. Boden, B. Boerner, S. Reich, The origin of high thermal conductivity and ultralow thermal expansion in copper-graphite composites, Nanolett. 15 (2015), 4745-4751.

14. A.M. Abyzov, F.M. Shakhov, A.I. Averkin, V.I. Nikolaev, Mechanical properties of a diamond-copper composite with high thermal conductivity, Mater. & Design 87 (2015), 527-539.

15. M. Schöbel, P. Dobron, J. Bernardi, R. Wimpory, K. Weidenmann, Elasto-plastic deformation within diamond reinforced metals for thermal management, Diamond and Related Mater. 70 (2016), 52-58.

16. C. Biao, K. Kondoh, Sintering behaviours of carbon nanotubes-aluminium composite powders, Metals 6 (2016), 213.

17. B. Boesl, D. Lahiri, S. Behdad, A. Agarwal, Direct observation of carbon nanotube induced strengthening in aluminium composite via *in situ* tensile tests, Carbon 69 (2014), 79-85.

19. X. Duan, Z. Yang, L. Chen, Z. Tian, D. Cai, Y. Wang, D. Jia, Y. Zhou, Review on the properties of hexagonal boron nitride matrix composite ceramics, J. Europ. Ceramics Soc. 36, 2016), 3725-3737.

20. K.L. Firestein, S. Corthay, A.E. Steinman, A.T. Matveev, A.M. Kovalskii, I.V. Sukhorukova, D. Golberg, D.V. Shtansky, High-strength aluminium-based composites reinforced with BN, AlB$_2$ and AlN particles fabricated via reactive spark plasma sintering of Al-BN powder mixtures, Mat. Sci. Eng. A 681 (2017), 1-9.

21. K.L. Firestein, A.E. Steinman, I.S. Golovin, J. Cifre, E.A. Obtaztsova, A.T. Matveev, A.M. Kovalskii, O.I. Lebedev, D.V. Shtansky, D. Golberg, Fabrication, characterization, and mechanical properties of spark plasma sintered Al-BN nanoparticle composites, Mat. Sci. Eng. A 642 (2015), 104-112.

22. D. Liu, H. Wen, D. Zhang, C. Wang, Y. Lin, Y. Xiong, T. Topping, J.M. Schoenung, E.J. Lavernia, Stress-enhanced grain growth in a nanostructures aluminium alloy during spark plasma sintering, Phil. Mag. Lett. 94 (2014), 741-748.

23. M. Anisimova, A. Knyazeva, I. Sevostianov, Effective thermal properties of an aluminum matrix composite with coated diamond inhomogeneities, Int. J. Eng. Sci. 106 (2016),142-154.

24. K. Mizuuchi, K. Inoue, Y. Agari, Y. Morisada, M. Sugioka, M. Tanaka, T. Takeuchi, J. Tani, M. Kawahara, Y. Makino, M. Ito, Thermal properties of Al/diamond composites fabricated in continuous solid-liquid co-existent state by SPS, Mater. Sci. Forum 706-709 (2012), 1967-1972.

25. N.B. Podymova, A.A. Karabutov, Combined effects of reinforcement fraction and porosity on ultrasonic velocity in SiC particulate aluminium alloy matrix composites, Composites Part B: Eng 113 (2017), 138-143.

21

applications, J. Europ. Ceramic Soc. 5 (1989), 3-9.

28. X. Liang, C. Jia, K. Chu, H. Chen, J. Nie, W. Gao, Thermal conductivity and microstructure of Al/diamond composites with Ti-coated diamond particles consolidated by spark plasma sintering, J. Composite Mater. 46 (2012), 1127-1136.

29. Y. Zhang, X. Wang, S. Jiang, J. Wu, Thermo-physical properties of Ti-coated diamond/Al composites prepared by pressure infiltration. Mater. Sci. Forum 654-656 (2010), 2572-2575.

30. M.H. Tsai, Physical properties of High Entropy Alloys, Entropy 15 (2013), 5338-5345.

31. Y.-F. Kao, S.-K. Chen, T.-J. Chen, P.-C. Chu, J.-W. Yeh, S.-J. Lin, Electrical, magnetic, and Hall properties of AlxCoCrFeNi high-entropy alloys, J. All. Compd. 509 (2011), 1607-1614.

32. S. Shafeie, S. Guo, Q. Hu, H. Fahlquist, P. Erhart, A. Palmqvist, High-entropy alloys as high-temperature thermoelectric materials, J. App. Phys. 118 (2015), 184905.

33. M.V. Novikov, A.L. Maistrenko, V.I. Kushch, S.A. Ivanov, Evaluation of the quality of composite diamond-containing materials by their electrical and thermal conductivity, Mater. Sci. 42 (2006), 113-120.

34. H.-P. Chou, Y.-S. Chang, S.-K. Chen, J.-W. Yeh, Microstructure, thermophysical and electrical properties in AlxCoCrFeNi (0≤x≤2) high-entropy alloys, Mater. Sci. Eng. B 163 (2009), 184-189.

35. Z. Fan, H. Wang, Y. Wu, X.J. Liu, Z.P. Lu, Thermoelectric high-entropy alloys with low lattice thermal conductivity, RSC Adv. 6 (2016), 52164-52170.

36. Y.S. Touloukian, R.K. Kirby, R.E. Taylor, P.D. Desai, Thermophysical properties of matter – The TPRC Data series. Volume 12: Thermal expansion of metallic elements and alloys, first ed., IFI/Plenum, New York, 1975.

Sci. Technol. 12 (2001), K1-K15.

38. É. Fazakas, V. Zadorozhnyy, L.K. Varga, A. Inoue, D.V. Louzguine-Luzgin, F. Tian, L. Vitos, Experimental and theoretical study of $Ti_{20}Zr_{20}Hf_{20}Nb_{20}X_{20}$ (X=V or Cr) refractory high-entropy alloys, Int. J. Refract. Metals Hard Mater. 47 (2014), 131-138.

39. A. Haglund, M. Koehler, D. Catoor, E.P. George, V. Keppens, Polycrystalline elastic moduli of a high-entropy alloy at cryogenic temperatures, Intermetal. 58 (2015), 62-64.

Sephira Riva,[1] Adam Tudball,[2] Shahin Mehraban,[1] Nicholas P. Lavery,[1] Stephen G.R. Brown,[1]

Kirill V. Yusenko[1*]

[1]College of Engineering, Swansea University, Bay Campus, Swansea SA1 8EN, Wales, UK

[2]Kennametal Manufacturing (UK) Ltd., Lake Road, Leeway Industrial Estate, Newport NP19 4SR,

Wales, UK

Correspondence:

Email: 839245@swansea.ac.uk (S.R.); k.yusenko@swansea.ac.uk (K.V.Y.)

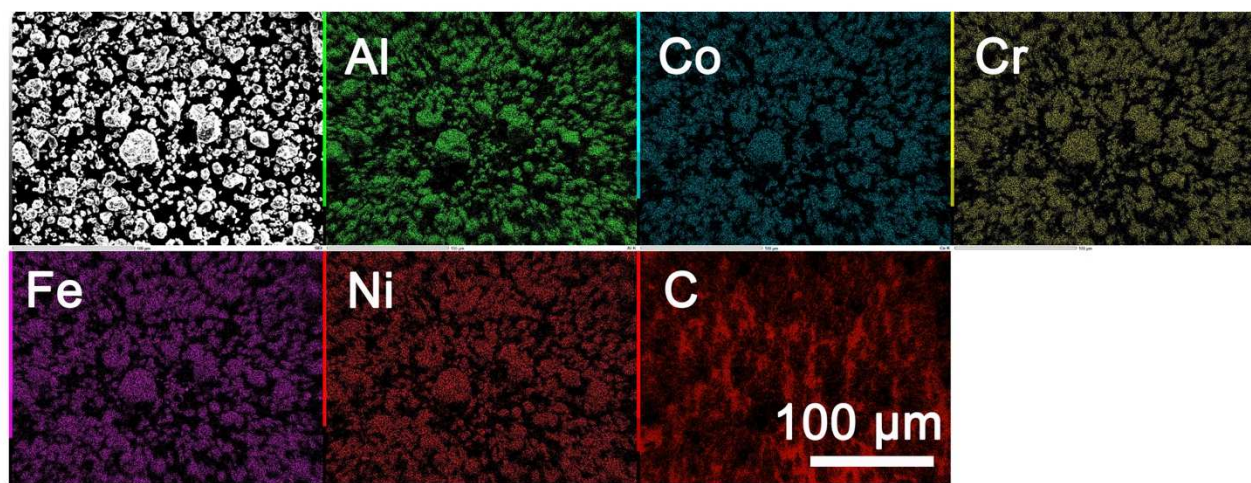Phone: +44 (0)1792205678 (K.V.Y.)

ELEMENTAL DISTRIBUTION OF THE BALL-MILLED POWDERS

Figure S1– $Al_2CoCrFeNi$ + 2 wt.% nanodiamonds after ball-milling with a Fritsch Planetary Mill PULVERISETTE 5/2 (10 mm steel balls, ball-to-powder ratio 5:1, 5 minutes, 250 r.p.m.).
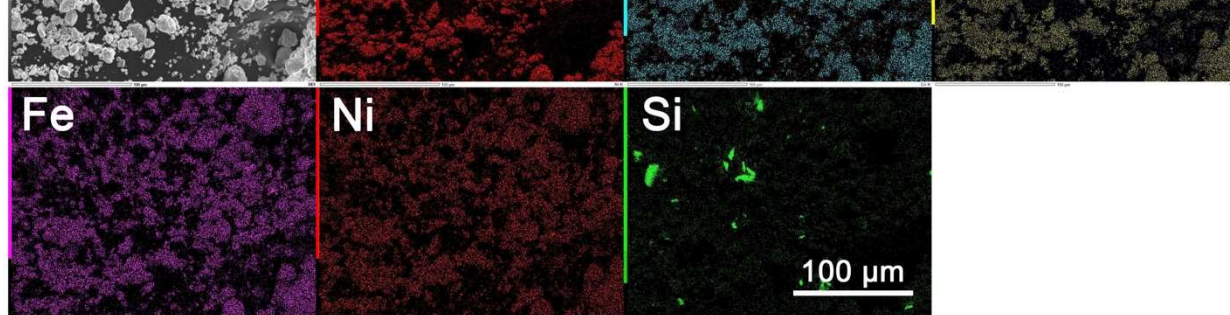
Figure S2 – Al$_2$CoCrFeNi + 2 wt.% SiC after ball-milling with a Fritsch Planetary Mill PULVERISETTE 5/2 (10 mm steel balls, ball-to-powder ratio 5:1, 5 minutes, 250 r.p.m.).
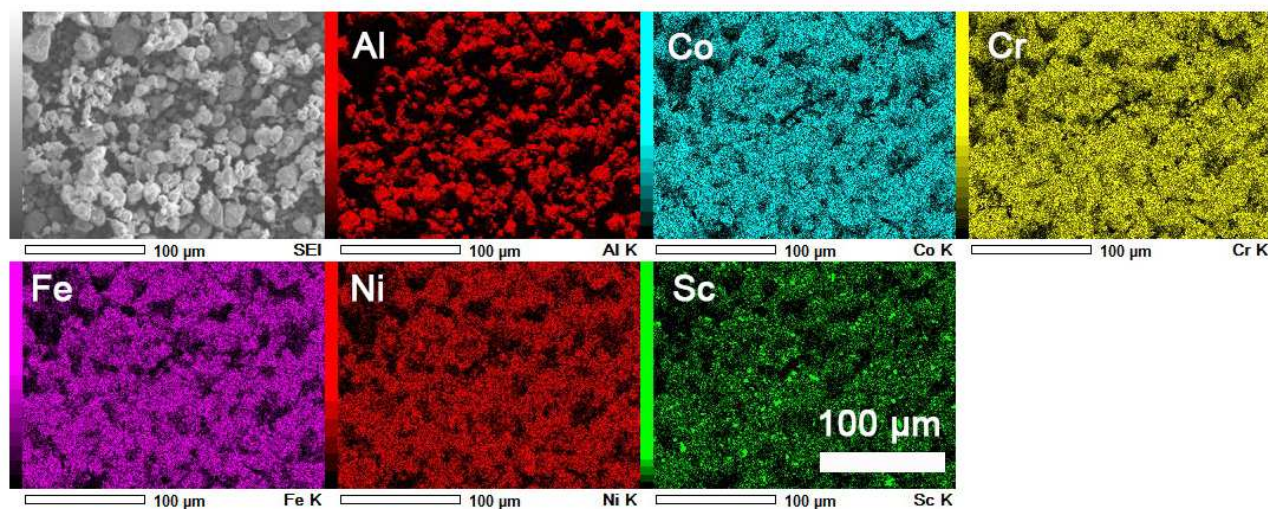

Figure S3 – Al$_2$CoCrFeNi + 0.5 wt.% Sc$_2$O$_3$ after ball-milling with a Fritsch Planetary Mill PULVERISETTE 5/2 (10 mm steel balls, ball-to-powder ratio 5:1, 5 minutes, 250 r.p.m.).
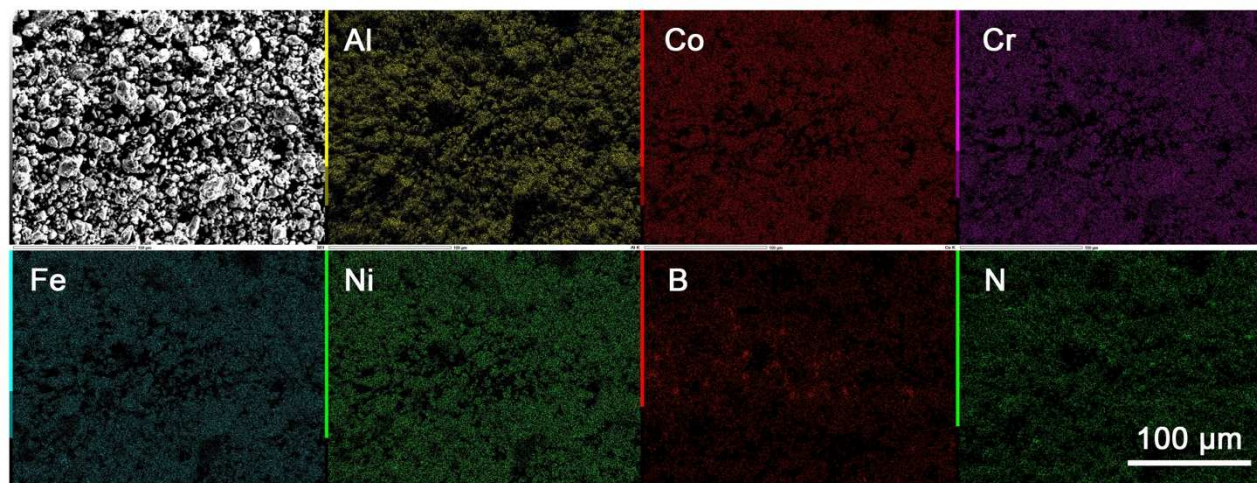

Figure S4 – Al$_2$CoCrFeNi + 3 wt.% *h*-BN after ball-milling with a Fritsch Planetary Mill PULVERISETTE 5/2 (10 mm steel balls, ball-to-powder ratio 5:1, 5 minutes, 250 r.p.m.).
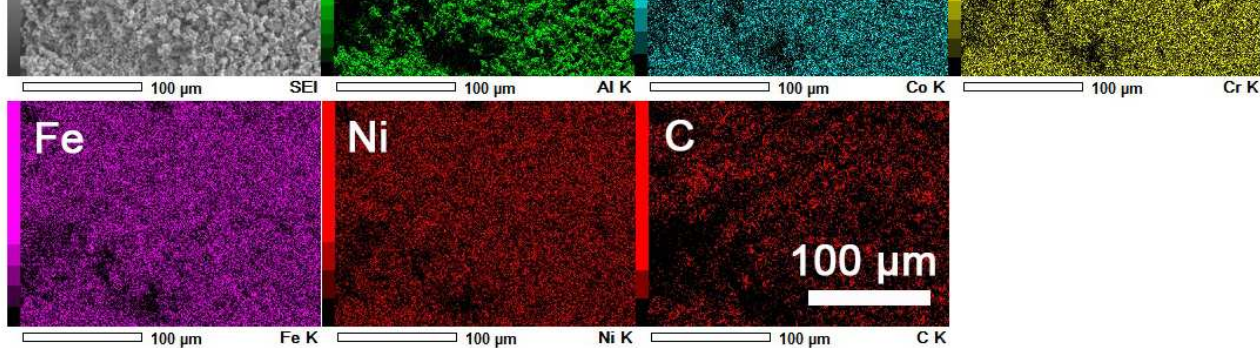
Figure S5 – Al$_2$CoCrFeNi + 1.5 wt.% CN after ball-milling with a Fritsch Planetary Mill PULVERISETTE 5/2 (10 mm steel balls, ball-to-powder ratio 5:1, 5 minutes, 250 r.p.m.).
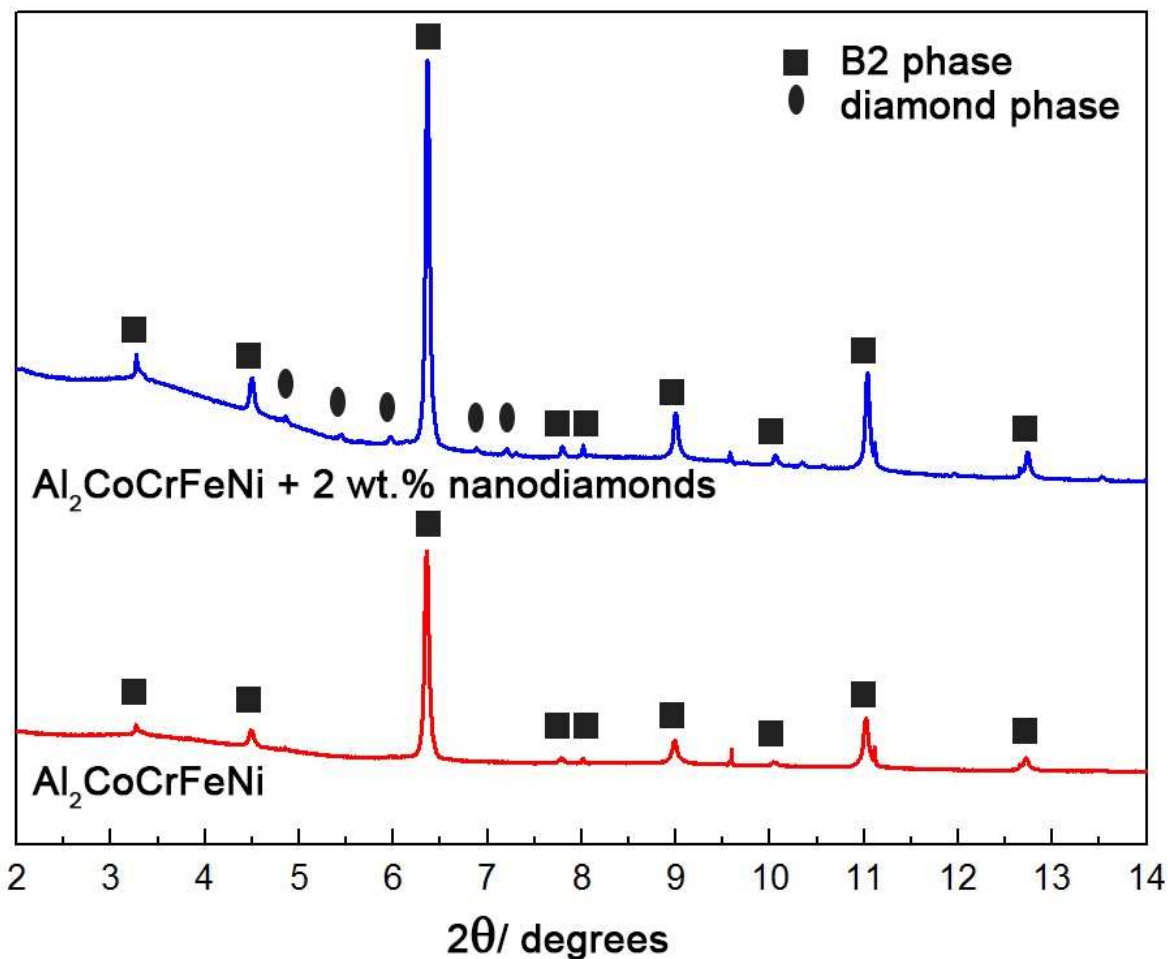
Fi

Figure S6 – PXRD of the Al$_2$CoCrFeNi (*red*) and Al$_2$CoCrFeNi+2 wt.% nanodiamond (*blue*) specimens. The B2 phase of the matrix and the diamond phase are highlighted. Performed at ID06 of ESRF (λ=0.22542 Å).